Published in final edited form as:

IEEE Trans Med Imaging. 2015 November ; 34(11): 2320–2332. doi:10.1109/TMI.2015.2430850.

Fiber Orientation and Compartment Parameter Estimation from Multi-Shell Diffusion Imaging

Giang Tran and

Department of Mathematics, University of California at Los Angeles, Los Angeles, CA 90095, USA

Yonggang Shi

Laboratory of Neuro Imaging (LONI), Mark and Mary Stevens Neuroimaging and Informatics Institute, Keck School of Medicine of University of Southern California, Los Angeles, CA 90033, USA

Giang Tran: giangtran@math.ucla.edu; Yonggang Shi: yshi@loni.usc.edu

Abstract

Diffusion MRI offers the unique opportunity of assessing the structural connections of human brains *in vivo*. With the advance of diffusion MRI technology, multi-shell imaging methods are becoming increasingly practical for large scale studies and clinical application. In this work, we propose a novel method for the analysis of multi-shell diffusion imaging data by incorporating compartment models into a spherical deconvolution framework for fiber orientation distribution (FOD) reconstruction. For numerical implementation, we develop an adaptively constrained energy minimization approach to efficiently compute the solution. On simulated and real data from Human Connectome Project (HCP), we show that our method not only reconstructs sharp and clean FODs for the modeling of fiber crossings, but also generates reliable estimation of compartment parameters with great potential for clinical research of neurological diseases. In comparisons with publicly available DSI-Studio and BEDPOSTX of FSL, we demonstrate that our method reconstructs sharper FODs with more precise estimation of fiber directions. By applying probabilistic tractography to the FODs computed by our method, we show that more complete reconstruction of the corpus callosum bundle can be achieved. On a clinical, two-shell diffusion imaging data, we also demonstrate the feasibility of our method in analyzing white matter lesions.

Index Terms

Multi-shell diffusion imaging; fiber orientation distribution; compartment models; white matter lesion

I. Introduction

With diffusion MRI, researchers can study the development and disruption of brain connectivity *in vivo*. One milestone in diffusion MRI is the development of diffusion tensor imaging (DTI) [1], which leads to highly popular measures such as fractional anisotropy

Correspondence to: Yonggang Shi, yshi@loni.usc.edu.

(FA) and enables streamline tractography for studying brain connectivity [2]–[7]. The tensor model, however, does not consider fiber crossings that are widely present in the brain [8], [9]. To overcome this limitation, various techniques were proposed to compute more detailed models of fiber orientations using high angular resolution diffusion imaging (HARDI) [10]–[21], which typically acquires data from a large set of gradient directions with a *single* b-value. With advances in MR imaging technologies [22], [23], in particular multiband acceleration [24]–[26], multi-shell diffusion MRI is becoming increasingly popular. Compared with conventional HARDI, multi-shell diffusion MRI acquires data with multiple b-values. As demonstrated by the public release of high resolution, multi-shell HARDI data from the Human Connectome Project (HCP) [27], [28], it is now practical to acquire multi-shell imaging data for large scale brain imaging studies and clinical research.

Multi-shell diffusion imaging can be viewed as an simplification of the diffusion spectrum imaging (DSI) [29]. Compared with the tensor model, DSI makes no assumption about the underlying microstructure and acquires data on a Cartesian grid in the q-space to fully recover the diffusion propagator at various locations of the brain, but its application in practical imaging studies is limited due to the need of long scanning time. To overcome this limitation, various multi-shell methods were developed to calculate the diffusion propagator from a much smaller set of gradient directions on several different b-values [30]–[33]. With the reconstructed diffusion propagator, more reliable estimation of the angular structure of diffusion profiles can be computed for brain connectivity analysis [34].

On the other hand, multi-shell imaging has also been used to study the brain microstructure with compartment modeling. With parametric representation of the diffusion imaging signals, compartment modeling has the potential of providing detailed characterization of brain microstructures with a much smaller dataset than DSI. The need of multiple compartments in analyzing diffusion MRI was first motivated by the observation of the non-monoexponential distribution of the diffusion imaging signal at high b-values [35], [36]. One important parameter of interest in the compartment model has been the axon diameter. For its estimation, highly demanding multi-shell imaging methods were proposed to study postmortem tissue samples [37]–[39] or anesthetized animals [40]. More practical acquisition schemes were developed recently to provide estimation of axon diameters and neurite distributions in human brain *in vivo* [41]–[44], but their applications are limited to brain regions with no fiber crossings. For the handling of more complicated fiber configurations, the ball-stick model was developed [45], [46], which uses the stick model for axonal diffusion and an isotropic diffusion compartment for extra-axonal diffusion. To better fit the multi-shell imaging data, the ball-stick model was extended with a gamma distribution of diffusivity [47], but it assumes the intra- and extra-axonal compartments have the same diffusivity. A comprehensive analysis of 47 possible combinations of compartment models were conducted recently [48], [49] and suggested three compartments were needed to accurately characterize signals from multi-shell imaging: intra-axonal compartment, extra-axonal compartment, and trapped water. While this study used only voxels with single fiber directions, its conclusion is valuable for studying brain regions with crossing fibers since we at least need the same number of compartments.

In this work, we develop a novel method for the analysis of multi-shell diffusion imaging data via the incorporation of compartment models into the spherical deconvolution framework in HARDI analysis. Spherical deconvolution is one of the most successful methods to resolve fiber crossings by computing the fiber orientation distribution (FOD) from diffusion imaging data. It has been applied to compute the FOD directly from the diffusion data [16] or the sharpening of the orientation distribution function (ODF) obtained from Q-ball imaging [19], [50]. For multi-shell imaging, spherical deconvolution was applied to process the ODF of generalized Q-ball imaging and obtain sharpened FOD, which is publicly available in the DSI-Studio software [50], [51]. For FODs represented with spherical harmonics, the extension of the spherical deconvolution approach to multi-shell data was proposed recently [52]–[54]. The focus of the work in [52], [53] were on enforcing the positivity of the FOD. In [54], the constrained spherical deconvolution (CSD) proposed in [16] was extended to multi-shell data with different diffusion kernels for white matter (WM), gray matter (GM), and cerebrospinal fluid (CSF) tissue, where the focus of introducing different kernels for the three tissue types is to provide more reliable FOD estimation on tissue boundaries. In contrast, the novel method we develop in this paper models the diffusion signal at the more detailed compartment level. For example, there should only be one WM component at voxels belonging to deep WM for the method in [54], but our method will estimate three compartments. The modeling approach between our method and [54] are also different. Similar to [16], the method in [54] used a data-driven approach and estimated all the kernels directly from the multi-shell imaging data. Once estimated, these kernels were fixed for the entire volume. On the other hand, our method is parametric and allows adaptive estimation of compartment parameters together with the FOD *at each voxel*. In addition, our method adaptively incorporates sparsity regularization and non-negativity constraints to avoid overly constraining the solution. By incorporating compartment models into the spherical deconvolution framework, our goal is to develop a more accurate characterization of multi-shell diffusion imaging signals from high b-values while retaining the capability of reliably representing crossing fibers.

Motivated by previous works on compartmental modeling of signals from multi-shell imaging [48], [49], we assume three compartments in our method to associate brain microstructure to the diffusion signal. For the signal from intra-axonal compartment, we model it as the spherical convolution of a stick kernel and the FOD. For the extra-axonal compartment, we model it as isotropic diffusion with an unknown diffusivity that we estimate as part of the solution. The third compartment represents the fraction of trapped water molecules with essentially negligible diffusion. While the full tensor model was also used in previous studies for modeling the extra-axonal compartment [48], [49], it could lead to underestimation of the intra-axonal compartment. This was shown to be a difficulty for some of the top ranked models studied in [49]. Because both the tensor (extra-axonal) and stick (intra-axonal) model are capable of explaining the anisotropy in the diffusion imaging signal, it is numerically challenging to accurately separate their contributions to the signal. Conventional ball-stick model does not have the third compartment and assumes the same diffusivity for the intra- and extra-axonal compartment, which has limited its performance in fitting the multi-shell data. Instead, our method decouples the diffusivity of the extra-axonal compartment from the stick kernel and allows it to be estimated adaptively. By using an

isotropic extra-axonal compartment that can change adaptively, we aim to achieve a balance between the complexity of the model and obtaining excellent fitting of the diffusion imaging signal. For the estimation of the FOD, the diffusivity of the extra-axonal compartment, and the fractions of each compartment, we develop a coordinate descent algorithm that solves a quadratic programming problem and a gradient descent step iteratively. Using HCP data, we show that our method can estimate FODs with ultra-sharpness. Besides the FOD, the diffusivity of the extra-axonal compartment represents another exciting result from our method because it provides excellent contrast between different tissue types. In comparisons with DSI-Studio and BEDPOSTX of FSL [47], we show that our method can generate more precise estimation of fiber directions in simulation studies, and cleaner and sharper FODs on real HCP data. With probabilistic tractography, we show that a more complete representation of the corpus callosum bundle can be reconstructed using FODs computed by our method. We also demonstrate the application of our method to clinical white matter (WM) lesion study using a two-shell, 45-direction data collected on a patient with multiple sclerosis.

A preliminary version of this work was published in a conference paper [52], where the focus was a novel way of introducing positivity constraints for FODs. Here we dramatically improve this work by incorporating compartment models into spherical deconvolution and develop an efficient numerical algorithm to solve for the FOD and compartment parameters. This new model provides a more faithful characterization of the diffusion signal and leads to sharp and clean FOD reconstruction. The rest of the paper is organized as follows. In section II, we develop the novel framework for FOD reconstruction with compartment modeling. An energy minimization method with adaptively selected constraints is then developed in section III to compute the FOD and compartment parameters. In section IV, experimental results from both simulated and real data will be presented to demonstrate the effectiveness of our method in the analysis of multi-shell diffusion imaging data. Finally, discussions and conclusions are made in section V.

II. FOD Estimation with Compartment Models

For the accurate reconstruction of brain connections from diffusion imaging data, we not only need to model fiber crossings with FODs, but also should properly model the different types of water diffusion in brain tissues and their contribution to the diffusion imaging signal. One important feature of our method is that we integrate the spherical deconvolution framework for FOD estimation with compartment models of water diffusion based on the underlying microstructure of brain tissues.

There are three compartments in our model to represent different types of water diffusion: intra-axonal diffusion, extra-axonal diffusion, and trapped water with negligible diffusion. The intra-axonal compartment accounts for water diffusion along the axons of WM fibers. Because the diameter of the axons are much smaller than the average water diffusion distance along the axon during the imaging process, the contribution of the radial diffusion is negligible [41], so we model the diffusion signal from the intra-axonal compartment with the stick model [43], [46], [48]:

$$k(b,u,w)=e^{-b\lambda_{\|}(u\cdot w)^2}, \quad (1)$$

where b is the b-value, u is the gradient direction, w is the fiber orientation, and $\lambda_{\|}$ is the diffusion coefficient along the axons. Following previous literature [43], we select this parameter as 0.0017 mm^2/s. In our experiments, we will show that reconstruction results from our method are robust to perturbations to this parameter. Let $\mathbb{S}$ denote the unit sphere and $f:\mathbb{S}\to\mathbb{R}^+$ denote the FOD. The contribution of the intra-axonal compartment to the diffusion signal is:

$$s_{IC}=f*_{\mathbb{S}}k, \quad (2)$$

where $*_{\mathbb{S}}$ denotes the spherical convolution of the FOD f and the stick kernel k.

The extra-axonal compartment takes into account the random water diffusion in the cellular environment outside the axon, including interstitial fluid, and we model it as isotropic diffusion with an unknown diffusivity. Let α be the fraction of the extra-axonal compartment. The contribution from this compartment to the diffusion signal is:

$$s_{EC}=\alpha\exp(-b\lambda_{iso}) \quad (3)$$

where λ_{iso} is the diffusion coefficient. Unlike the intra-axonal compartment, the cellular environment of the extra-axonal compartment could depend upon fiber configurations, we thus model λ_{iso} as an unknown parameter to be estimated from the data. This also helps account for the different isotropic diffusions in the cerebrospinal fluid (CSF) and the extra-axonal compartment of the gray matter (GM) and WM regions.

The third compartment models water molecules trapped inside cell bodies surrounding axons with negligible diffusion [48]. We represent its contribution to the diffusion signal as a constant γ.

Let $s(b, u)$ denote the diffusion signal at the b-value b and the unit direction u at a voxel. By combining the contributions from the three compartments, the diffusion signal can be expressed as:

$$s(b,u)=f*_{\mathbb{S}}k+\alpha e^{-b\lambda_{iso}}+\gamma+n \quad (4)$$

where n denotes the noise in the signal. The sum of all compartment fractions satisfies the *normalization condition*:

$$\int_{\mathbb{S}} f dw+\alpha+\gamma=1. \quad (5)$$

The overall goal is to reconstruct the FOD f and the compartment parameters α, λ_{iso}, γ from diffusion imaging data at each voxel.

For efficient computation, we represent the FOD with the spherical harmonics (SPHARMs) up to the order L:

$$f(w)=\sum_{l,m} x_l^m Y_l^m(w) \quad \forall w \in \mathbb{S} \tag{6}$$

where Y_l^m is the *m*-th real SPHARM basis at the order $l = 0, 2, \cdots, L$, and x_l^m is the coefficient for the basis Y_l^m. Note that only even order SPHARMs are used because the FOD is symmetric on the sphere. For simplicity, we denote Y_l^m and x_l^m by Y_j and x_j, respectively, with $j=m+\frac{l^2+l+2}{2}$. Using the Funk-Hecke theorem, we can express the signal from the intra-axonal compartment as follows:

$$\begin{aligned} f *_{\mathbb{S}} k &= \int_{\mathbb{S}} \sum_j x_j Y_j(w) e^{-b\lambda_{\parallel}(u\cdot w)^2} dw \\ &= \sum_j Y_j(u) G_l(b, \lambda_{\parallel}) x_j, \end{aligned} \tag{7}$$

where $G_l(b, \lambda_{||})$ is defined as:

$$G_l(b, \lambda_{\parallel}) = 2\pi \int_{-1}^{1} P_l(t) e^{-b\lambda_{\parallel} t^2} dt. \tag{8}$$

Here P_l is the Legendre polynomial of degree *l*.

Let $\underline{s}$ denote the vector of diffusion signals $s(b_i, u_i)$ sampled at the *b*-values b_i and the unit directions u_i, ($i = 1, \cdots, N$), where *N* is the number of measured signals. Given the maximum order *L* of the SPHARMs used, the total number of basis functions is $J = (L + 1)(L + 2)/2$. Let $\underline{x} = [x_1, \cdots, x_j, \cdots, x_J]^T$ be the vector of coefficients for the FOD, we can write (4) in the matrix form as:

$$\underline{s} = A\underline{x} + \alpha\underline{\beta} + \gamma\underline{e} + \underline{n} \tag{9}$$

where the matrix $A = Y \cdot G$ is the entry-wise product of two matrices *Y* and *G* defined as follows:

$$Y = \begin{bmatrix} Y_1(u_1) & Y_2(u_1) & \cdots & Y_J(u_1) \\ Y_1(u_2) & Y_2(u_2) & \cdots & Y_J(u_2) \\ \cdots & \cdots & \cdots & \cdots \\ Y_1(u_N) & Y_2(u_N) & \cdots & Y_J(u_N) \end{bmatrix} \tag{10}$$

$$G = \begin{bmatrix} G_0(b_1) & G_2(b_1) & \cdots & G_2(b_1) & \cdots & G_L(b_1) \\ G_0(b_2) & G_2(b_2) & \cdots & G_2(b_2) & \cdots & G_L(b_2) \\ & & & \cdots & & \\ G_0(b_N) & G_2(b_N) & \cdots & G_2(b_N) & \cdots & G_L(b_N) \end{bmatrix}. \tag{11}$$

In the *i*-th row of the matrix *G*, the matrix element $G_l(b_i) = G_l(b_i, \lambda_{||})$, with *l* from 0 to *L*, is repeated $2l+1$ times. In (9), α is the unknown fraction of the extra-axonal compartment, the product of α and $\underline{\beta} = [\ e^{-b_1\lambda_{iso}} \quad e^{-b_2\lambda_{iso}} \quad \cdots \quad e^{-b_N\lambda_{iso}}\ ]^T$ is the signal from this

compartment. The signal from the trapped water compartment is written as the product of the unknown fraction γ and the vector $\underline{e}=[\ 1\quad 1\quad \cdots\quad 1\ ]^T$. Finally $\underline{n}$ denotes the vector of noise.

III. Adaptively Constrained Energy Minimization

For the reconstruction of FOD and compartment parameters, we develop in this section a constrained energy minimization approach. Among the constraints, the non-negativity of FOD is the most challenging to satisfy under the SPHARM representation because practically we can only afford to use a finite set of SPHARM basis. To overcome this difficulty, we develop an adaptive strategy to limit the negative components to the minimal extent while ensuring major fiber directions are captured accurately. After that, we formulate the constrained energy minimization framework and develop an iterative algorithm to obtain the solution for the FOD and compartment parameters.

Our strategy is to constrain the FOD to be non-negative on a *minimal* set of *uniformly* distributed points on the sphere. The key idea is the adaptive selection of the set of constraints for every voxel to avoid overly constraining the solution and affecting reconstruction accuracy. With a remeshing algorithm [55], we build a collection of constraint sets $\mathscr{V} = \{V_1, V_2, \cdots,\}$ with varying number of points on the sphere, where each member $V_M=\{v_M^1, v_M^2, \cdots, v_M^M\}$ is a set of M uniformly distributed points on the hemisphere of the unit sphere. Under the SPHARM representation, the requirement that the FOD f should be non-negative on V_M can be expressed as:

$$C_M \underline{x} \geq 0 \quad (12)$$

where C_M is a matrix of size $M \times J$ defined as

$$C_M = \begin{pmatrix} Y_1(v_M^1) & Y_2(v_M^1) & \cdots & Y_J(v_M^1) \\ Y_1(v_M^2) & Y_2(v_M^2) & \cdots & Y_J(v_M^2) \\ \cdots & \cdots & \cdots & \cdots \\ Y_1(v_M^M) & Y_2(v_M^M) & \cdots & Y_J(v_M^M) \end{pmatrix}.$$

With the FOD being non-negative on a set of uniformly distributed points, we ensure that large negative components will not occur and most of the energy of the FOD are contributed by physically meaningful, i.e., positive, components.

In our constrained minimization framework, we define an energy function that consists of a data fidelity term and a regularization term for the sparsity of the FOD:

$$E(\underline{x},\alpha,\lambda_{iso},\gamma)=\frac{1}{2}\|\underline{s}-A_+\begin{bmatrix}\underline{x}\\ \alpha\\ \gamma\end{bmatrix}\|^2+\xi\int_{\mathbb{S}} f dw$$
$$=\frac{1}{2}\|\underline{s}-A_+\begin{bmatrix}\underline{x}\\ \alpha\\ \gamma\end{bmatrix}\|^2+\xi I\underline{x}.$$

The first part of the energy is the data fidelity term. Following (9), the matrix A_+ is defined as

$$A_+=[\ A\quad \underline{\beta}\quad \underline{e}\ ]. \quad (13)$$

Note that if we only have data from one *b*-value, the first and last two columns of the matrix are co-linear, so there is ambiguity to distinguish the constant component of FOD and the compartment parameters. This shows mathematically the importance of using multi-shell imaging for accurately resolving fiber orientation and compartment parameters. The second term penalizes the L_1 energy of the FOD to encourage its sparsity. Because the integral of all SPHARM basis of order greater or equal to one is zero, we have the matrix representation of the L_1 term with the matrix $I=[\ \sqrt{4\pi}\quad 0\quad \cdots\quad 0\ ]$.

Given the constraint set and regularization parameter ξ, we have a constrained energy minimization framework for FOD reconstruction and compartment parameter estimation:

$$\begin{aligned}\min\quad & E(\underline{x},\alpha,\lambda_{iso},\gamma)\\ \text{s.t.}\quad & \begin{cases} I\underline{x}+\alpha+\gamma=1\\ C_M\underline{x}\geq 0\\ \alpha\geq 0\\ \lambda_{iso}\geq 0\\ \gamma\geq 0.\end{cases}\end{aligned} \quad (14)$$

The first normalization constraint represents that WM and non- WM tissue fractions need to sum to unity. The second, third, and fourth constraints are for non-negativity of the FOD and compartmental parameters.

To solve this problem, we develop a coordinate descent algorithm that cycles through a quadratic programming step and a gradient descent step. In the first step, we compute the FOD, i.e., $\underline{x}$, and the compartment parameters α and γ via the solution of a constrained quadratic programming problem given the parameter λ_{iso}:

$$\begin{aligned}\min\quad & \frac{1}{2}\|\underline{s}-A_+\begin{bmatrix}\underline{x}\\ \alpha\\ \gamma\end{bmatrix}\|^2+\xi I\underline{x}\\ \text{s.t.}\quad & \begin{cases} I\underline{x}+\alpha+\gamma=1\\ C_M\underline{x}\geq 0,\alpha\geq 0,\gamma\geq 0.\end{cases}\end{aligned} \quad (15)$$

For the numerical implementation of this step, we use the software package QPC [56] to obtain the solution.

In the second step, we fix the parameters $\underline{x}$, α, γ, and update λ_{iso} in the gradient descent direction. The gradient of the energy with respect to λ_{iso} is defined as follows:

$$\frac{\partial E}{\partial \lambda_{iso}} = -\left(\underline{s} - A_+ \begin{bmatrix} \underline{x} \\ \alpha \\ \gamma \end{bmatrix} \right)^T \frac{\partial \underline{\beta}}{\partial \lambda_{iso}} \alpha \quad (16)$$

where

$$\frac{\partial \underline{\beta}}{\partial \lambda_{iso}} = \begin{bmatrix} -b_1 e^{-b_1 \lambda_{iso}} & -b_2 e^{-b_2 \lambda_{iso}} & \cdots & -b_N e^{-b_N \lambda_{iso}} \end{bmatrix}^T \quad (17)$$

We calculate the energy in (14) at each iteration and determine convergence is reached if the energy stops decreasing. By cycling these two steps until convergence, we obtain the FOD reconstruction and compartment parameters.

To obtain satisfactory reconstruction results, it is critical to develop an intuitive mechanism for the proper selection of the two important parameters in our method: the non-negative constraint set and the regularization parameter. Because the complexities of fiber crossings are spatially varying across the brain, the number of active constraints in (12) could be different as a result. Thus we adaptively search through the constraint collection $\mathscr{V}$ at every voxel to find the smallest M such that the FOD solution satisfies:

$$\frac{\int_{f(w)>0} f dw}{\int_{f(w)<0} |f| dw} > \delta_P, \quad (18)$$

where the parameter δ_P is straightforward to pick. This condition measures how successful the reconstructed FOD is able to focus its energy on positive components. For example, if we pick $\delta_P = 25$, we ensure more than 95% of the L_1 energy of the FOD are from positive components. As a demonstration, we show in Fig. 1 the FOD reconstruction results of two fibers using simulated diffusion data according to the three-shell, 270-direction scheme of HCP. For the results in Fig. 1 (a) and (b), the maximum order of SPHARM used here is L = 8. The result in Fig. 1 (a) is obtained from adaptively determined constraints, where M = 69, and the result in Fig. 1 (b) is obtained by fixing M = 100. We can see that it is much harder to recover the true fiber directions from the overly constrained solution. From a tractography point of view, the overly constrained solution will lead to more false positives in probabilistic tractography. The number of constraints also depends on the maximum SPHARM order used in the reconstruction. With the use of higher order SPHARMs, we can reconstruct sharper FODs given data from a sufficient number of gradient directions, but this requires a larger number of constraints to ensure the non-negativity condition is satisfied. In Fig. 1(c), we show the reconstruction result with L = 16, where the adaptively determined number of constraints is 216. We can see a much sharper FOD is computed. For practical implementation, there is no need to start the search from M = 1. Given a maximum order L,

we can pick a constraint set from experience and start the search there. For $L = 8$, we typically start the search at $M_{init} = 60$. For $L = 16$, we can start the search at $M_{init} = 200$.

For the selection of the regularization parameter ξ, we use an explicit measure of FOD sparsity. Let K_{MAX} denote the maximum number of fiber crossings allowed in each voxel, which we typically choose as $K_{MAX} = 4$. At each voxel we denote $P = \{p_1, p_2, \cdots, p_K\}$ as the set of maximal peaks of the FOD such that $f(p_1) \geq f(p_2) \geq \cdots \geq f(p_K)$. With the SPHARM representation, the FOD is a smooth function defined on a triangular mesh representation of the sphere. We detect each maximal peak of the FOD as a vertex with its FOD value greater than that of its one-ring neighbors. Let δ_F denote the threshold for fiber sparsity. We define the *fiber sparsity condition*:

$$\exists 1 \leq K^* K_{MAX} \quad s.t. \quad \frac{\sum_{k=1}^{K^*} f^2(p_k)}{\sum_{k=1}^{K} f^2(p_k)} > \delta_F. \quad (19)$$

The parameter δ_F determines the lower bound of the ratio between the l^2 energy of the first K^*largest peaks and the total l^2 energy of all peaks. This is an intuitive measure that can be picked easily. In our experiments, we fix $\delta_F = 0.99$. By checking the fiber sparsity condition, we can determine if the parameter ξ is large enough. If there are too many spurious peaks that fails the condition in (19), we increase ξ and this will push down the constant term of the FOD, i.e., $I\underline{x}$. As a result, the FOD solution has to change to meet non-negativity constraints and more energy will be pushed toward the other two compartments due to the normalization condition.

In summary, we have listed the overall reconstruction algorithm in Table I. At the start of the algorithm, we set ξ and M as the initial values ξ_{init} and M_{init} that depend on the SPHARM order used and number of gradient directions. We first set an initial value $\lambda_{iso} = 0.001\ mm^2/s$ and solve (15) repeatedly with increasing M to meet the non-negativity condition in (18). After that, we run the coordinate descent steps of quadratic programming in (15) and gradient descent update of λ_{iso} in (16). If convergence is reached, we check if the sparsity condition in (19) is satisfied. If so, we stop the algorithm; otherwise, we increase the regularization parameter ξ with a step size δ_ξ and repeat the above steps.

IV. Experimental Results

In this section, we present experimental results to demonstrate our reconstruction algorithm. In our experiments, we mainly focus on the application of our method to diffusion imaging data from the HCP since they are publicly available and there are wide interests in analyzing these data. The diffusion MRI data from HCP were acquired from 270 gradient directions on three shells with b-values: $1000 s/mm^2$, $2000 s/mm^2$, and $3000 s/mm^2$. We will first compare our method with DSI-Studio and the BEDPOSTX tool of FSL, which implements the multi-shell extension of the ball-stick model [47], on simulated data to quantify angular accuracy in the reconstructed FODs and test the reliability of our method in estimating compartment parameters. After that, we will apply all three methods to a real HCP dataset and compare the reconstructed FODs. Using FODs computed by our method from the HCP data, we present results on automated fiber bundle extraction in the third experiment. Finally, we will

present FOD reconstruction results using data from a two-shell, 45-direction clinical scan we collected on a 3T GE scanner. In particular, we will illustrate the potential of our method in studying WM lesions in neurological diseases.

A. Simulation results

In the first experiment, we test our method on simulated data using the same gradient table of HCP imaging protocol. The fiber configurations used in the simulation are shown in Fig. 2, where five types of fiber configurations are simulated: single fiber, two fibers crossing at 90º, 60º, 45º, and three fibers crossing at 60º. The simulated intra-axonal, extraaxonal, and trapped water fractions are: 0.35, 0.5, 0.15. The mean diffusivity of GM regions calculated by tensor-based analysis of HCP data is typically around 0.0007 mm^2/s. Assuming there are less obstruction for water diffusion in the extra-axonal compartment of the WM regions than the GM regions that consist of highly packed cell bodies, we pick the diffusivity of the extra-axonal compartment in our simulation as 0.0012 mm^2/s, which is the mean value of the GM diffusivity and the diffusivity of our stick kernel for the intra-axonal compartment. This value is also comparable to the diffusivity of WM regions estimated by the ball-stick model of FSL with HCP data. As noted in section II, we fix the parameter $\lambda_{||} = 0.0017\ mm^2/s$ in our reconstruction process. To test the robustness of our method to this parameter, we randomly sample it in the range (0.0015, 0.0019) mm^2/s in the simulation for each voxel. Given the fiber configurations and compartment parameters, we generate the simulated signal according to (4). We will show in the next experiment that it produces synthesized signals fitting excellently with real data. At each voxel, two different levels of Rician noise were added to each signal from the 270 gradient directions to generate two sets of signals with SNR=10 and SNR=5. Let $\underline{s}_{clean} \in \mathbb{R}^N$ denote a set of clean signals from N gradient directions and $|\underline{s}_{clean}|$ denote the mean magnitude of the clean signals. Given an SNR level, we added Rician noise to generate the noisy signal $\underline{s}$ as follows:

$$\underline{s} = \sqrt{(\underline{s}_{clean} + \underline{n})^2 + (\underline{n})^2},$$

where $\underline{n} \in \mathbb{R}^N$ is a vector of zero mean Gaussian noise with standard deviation σ defined as $\sigma = |\underline{s}_{clean}|/(\sqrt{2}\, SNR)$.

For comparisons, we applied our method, DSI-Studio [50], [51] and BEDPOSTX of FSL [47] to the simulated data. DSI-Studio is publicly available and can efficiently compute sharpened FODs from arbitrary acquisition schemes. In our method, we discretized the unit sphere with a mesh of 2562 vertices and choose the SPHARM order $L = 16$. The step size in updating the sparsity regularization was chosen as $\delta_\xi = 0.1$. For DSI-Studio, we choose the 16 fold discretization level to obtain the same number of vertices in discretizing the sphere. BEDPOSTX solves the ball-stick model with multi-shell diffusion imaging data by incorporating a gamma distribution of diffusivity. Instead of computing a continuous FOD, BEDPOSTX generates a set of sampled fiber directions as the solution that can be used for fiber tractography. For all three methods, we selected the maximum allowed number of fiber directions in each voxel as 4. On a PC with a 2.7GHz Intel CPU, it took our method around 60 seconds and DSI-Studio around 90 seconds to compute the 121 FODs of the simulate

image. For BEDPOSTX, it took around 300 seconds to compute the solution for the 121 voxels.

For the voxels enclosed by the red dashed lines in Fig. 2, we plotted the FOD reconstruction results by our method in Fig. 3(a) and (d) from the two sets of signals at SNR=10 and 5. For the same set of voxels, the FODs reconstructed by DSI-Studio are plotted in Fig. 3 (b) and (e). To visualize the results from BEDPOSTX in a similar way, we plotted each sampled fiber direction as a line segment with the same color coding scheme used for plotting the FODs. The length of each line segment is in proportion to its corresponding volume fraction generated by BEDPOSTX. The results for SNR=10 and 5 were plotted in Fig. 3 (c) and (f). Compared with DSI-Studio, we can see that our method can produce sharper FODs with much better ability of resolving fiber crossings, especially in the cases of the two fibers crossing at 45º and the three fiber crossing at 60º. While BEDPOSTX can also generate very sharp fiber direction distributions, we can see that it tends to generate more false positives than our method. The false positives that can be seen most easily are those line segments plotted in red in Fig. 3 (c) and (f). They do not exist in the true fiber directions or our results. At SNR = 5, the difference between our method and BEDPOSTX are more evident. As shown in Fig. 3 (d) and (f), we can see the results from BEDPOSTX are more dispersed as compared to the FODs computed by our method.

For a more quantitative evaluation, we calculated the *average angular error* (AAE) for all the 121 voxels in Fig. 2. For our method and DSI-Studio, we compute the AAE as follows. At each voxel, we first calculate the angular error of each vertex on the unit sphere, where the FOD is defined, with respect to the nearest true fiber direction shown in Fig. 3 (a). The AAE of the FOD at this voxel is then defined as the weighted average of the angular error at each vertex, where the weight is the FOD value at each vertex. The AAE for results from BEDPOSTX were computed similarly. For each sampled fiber direction, we computed its angular error with respect to the nearest true fiber direction. The AAE at each voxel is then the weighted average of the angular error of all sampled fiber directions with the weight defined as their corresponding volume fractions generated by BEDPOSTX. Note that this definition of angular error characterizes the actual errors in probabilistic tractography. The mean and standard deviation of the AAE from our method, DSI-Studio and BEDPOSTX are listed in Table II. For all three methods, smaller AAE was achieved with higher SNR in the signal. This is important for reducing false positives in FOD-based tractography and improving the accuracy in modeling brain connectivity. Overall a comparison of the results from the three methods confirms that our FOD reconstruction method achieves better performance in accurately modeling fiber orientations.

Besides the angular errors, we also calculated the mean and standard deviations of the errors in the compartment parameters estimated by our method. The results are listed in Table III. Similar to the AAE results, we see higher SNR leads to more accurate estimation of the compartment parameters. At SNR=10, we can see the mean of the errors are almost two orders of magnitude smaller than the true value of the compartment parameter, and the standard deviation of the errors at SNR=10 are at least an order of magnitude smaller than the true value of the corresponding parameter. The results at SNR=5 are only slightly worse as can be seen from their larger standard deviations than the results at SNR=10. Overall we

can see that our method produces very accurate estimation of compartment parameters, which can be valuable for the early detection and characterization of brain tissue pathology in various neurological disorders. One such example will be presented in section IV-D to illustrate the application of our method in studying white matter lesions.

In summary, the results from the simulation show that our method not only accurately reconstructed the FODs, but also reliably estimated the compartment parameters.

B. HCP data results

In the second experiment, we present reconstruction results from the multi-shell diffusion imaging data of one HCP subject. For this real data, we use the same set of parameters as in the simulation experiment for both our method and DSI-Studio.

To demonstrate that our three-compartment model provides an accurate characterization of the diffusion imaging signal, we used the reconstructed FODs and compartment parameters to calculate the synthesized signal with (4) for all the 270 gradient directions on three shells with b-values: 1000 s/mm^2, 2000 s/mm^2 and 3000 s/mm^2, and compare them with the real signal. For two representative voxels with two and three crossing fiber directions, we overlaid the synthesized signals over the real signal from each b-value in Fig. 4 (a) and (b). Note that the x-axis in the figures represent the index of the gradient directions that we ordered according to the magnitude of the synthesized signal for each b-value. The excellent match shows that our model provides a nice fitting of the multi-shell diffusion imaging signals. For a more detailed demonstration of how well our compartment modeling matches diffusion signals, we calculated the residue between the real signal and the signal synthesized from the reconstruction results according to our model. The ratio between the norm of the residue and the real signal is plotted on an axial slice in Fig. 4(c), which shows that the brain regions have an overall ratio of around or below 0.1 except ventricles or other regions containing CSF. This corresponds to a signal to residue ratio (SRR) of 10 that matches the SNR of the HCP data very well, which is also around 10 [23]. The low SRR in the CSF is expected because the signals in these regions are highly attenuated due to the free diffusion of the water.

For three ROIs shown in Fig. 5 that are representative of different types of brain regions, we plotted in Fig. 6 the FODs reconstructed by our method and DSI-Studio, and fiber directions computed by BEDPOSTX of FSL to compare their performance. ROI I shown in Fig. 5(a) is in the WM region where the corpus callosum and the corticospinal tract meet. ROI II shown in Fig. 5(b) is in the thalamus which consists of a mix of GM, dendrites and myelinated axons. ROI III shown in Fig. 5 (b) is on the boundary of GM and WM. For all three ROIs, we can see that our method computes sharper and cleaner FODs than DSI-Studio. The fiber direction distribution computed by BEDPOSTX were plotted in the same way as in Fig. 3. As shown in Fig. 6(c), BEDPOSTX is able to compute a very sharp distribution of fiber directions in many voxels, but it also generates very dispersed results for voxels on the top left corners and the middle of the fourth and fifth rows as compared to our results shown in Fig. 6 (a). This is consistent with its tendency of generating false positives that we observed in the simulation experiment. This trend is even more obvious for ROI II in the thalamus. By comparing the results in Fig. 6 (d) and (f), we can see our method is able to produce sharper

distributions of fiber directions than BEDPOSXT in this challenging region. ROI III represents the transition from WM into GM regions when we go from its left to the right side. As shown in Fig. 6 (g), (h), (i), we can see the FODs reconstructed by all three methods become “fatter” for voxels closer to the GM, which represents more dispersed fiber directions as axons project to the cortex. On the other hand, we can see our method still produces much cleaner fiber direction distributions than BEDPOSTX. Voxels on the lower right corner of the ROI III belong to the CSF region. We can see that our method computes FODs with almost negligible magnitude while DSI-Studio and BEDPOSTX produces results with magnitudes that are not consistent with the underlying anatomy.

For the HCP subject, the compartmental fractions and the diffusivity of the extra-axonal compartment are plotted in Fig. 7 on an axial and coronal slice. In WM regions with only one fiber direction such as the corpus callosum and corticospinal tract, we can see they have higher intra-axonal fractions. Lower intra-axonal fractions are observed in areas with fiber crossings such as locations where the corpus callosum and the corticospinal tract meet. In the thalamus we also see a lower intra-axonal fraction than whiter matter regions. Most interestingly, we see the diffusivity of the extra-axonal compartment shown in Fig. 7 (d) has the power of differentiating tissue types in the brain. The CSF region has the highest diffusivity. The cortical and sub-cortical GM regions both have lower diffusivity than the WM region, possibly due to the more tightly packed cell bodies in these regions. There is also large variability across different WM regions. For the extra-axonal compartment, we observe higher diffusivity in regions with mostly a single-fiber configuration and lower diffusivity in regions with complicated fiber crossings, possibly due to more obstruction for water diffusion in these regions.

C. Fiber bundle from HCP data

For all the multi-shell data of 215 subjects released in the first three quarters by HCP, we have successfully applied our method to reconstruct FODs with the maximum SPHARM order at 16. Using probabilistic tractography, these whole brain FODs allow the construction of high quality fiber bundles with unprecedented details. As a demonstration, we present results on the automated extraction of the corpus callosum (CC) bundle in the third experiment.

As shown in Fig. 8(a), the ROIs used in our CC bundle reconstruction include the following regions computed from the T1-weighted structural MR image: the CC region in the middle sagittal slices, the precentral gyrus of the left and right hemisphere. Using the algorithm in [57], [58], we first automatically reconstructed the cortical surfaces from the T1- weighted MR image and parcellated them into gyral labels defined in the LPBA40 atlas [59]. The gyral labels were then extended to voxels within 4mm of the surface using the fast marching algorithm [60]. To identify the CC region in middle sagittal slices, we found voxels that satisfied the following conditions: distances to left and right hemisphere surfaces are both below 3 voxels; the maximum magnitude of its FOD is greater than 0.5; the fiber direction that achieves the maximum FOD magnitude best aligns with the x-axis instead of the y-and z-axis. For all the voxels satisfying these conditions, we used the largest connected component as the CC region.

To find the CC bundle that connects the left and right motor cortex, we used the three ROIs as seed regions and ran FOD-based probabilistic tractography with the MRTrix software [7]. Only tracts that passed through all three regions were kept in the reconstructed bundle. In Fig. 8, we plotted the bundles from 5 HCP subjects to illustrate the performance of our method. Compared with CC bundles shown in previous literature that usually exhibit a U-shape [61], [62], our results provide a much more complete reconstruction of the projection of the CC bundle to the lateral cortices. To demonstrate that improved CC bundle reconstruction is indeed due to FOD-based analysis, we calculated the number of fiber directions at each voxel that the fiber bundle passes through using the peaks of the reconstructed FOD. For rigorousness, only major peaks with a magnitude above 0.1 are considered here. Because FODs are symmetric with respect to the origin of the unit sphere, we divide the number of peaks by two to obtain the number of fiber directions at each voxel and denote the result as the peak image. For the fiber bundle in Fig. 8 (b), we plotted the overlay of the bundle and its peak image in Fig. 9 (a) and (b). Note that the plots show only the intersection of one coronal slice of the peak image with the 3D fiber bundle, but they clearly show the need of FOD-based analysis in order to capture the lateral projection of the CC bundle. Quantitatively more than 60% of the voxels that the reconstructed CC bundle passes through contain crossing fibers. For all five subjects, the statistics about their peak images are listed in Tabel IV. We can see the results are highly consistent across subjects and demonstrates the need of FOD-based tractography for the improved analysis of human brain connections.

D. Clinically feasible multi-shell imaging

The multi-shell, 270-direction data from HCP provides us a great opportunity to study brain connectivity, but it requires several hours of scanning time on regular 3T MR scanners that are not practical for clinical uses. In this experiment, we demonstrate the application of FOD-based analysis for clinically feasible, multi-shell diffusion imaging. The MR images used in this experiment was acquired from a patient with multiple sclerosis (MS) on a 3T GE scanner. The data used in this experiment include the T2-FLAIR image, and diffusion MRI acquired from 45 gradient directions on two different shells. The b-value of the first shell is $1000 s/mm^2$ and it has 25 gradient directions. The b-value of the second shell is $2000 s/mm^2$ and it has 20 gradient directions.

For the detection of WM lesions, T2-FLAIR is a popular choice in clinical practice. As shown in Fig. 10 (a), we highlighted one lesion inside the red box on an axial slice of the T2-FLAIR image. For the two-shell diffusion imaging data on this MS patient, we applied our method to reconstruct the FODs at the SPHARM order 12. For the highlighted ROI, the FODs were overlaid with the T2-FLAIR image in Fig. 10(b). From the results we can see that our method is able to reconstruct sharp and clean FODs with consistent orientations among neighboring voxels. With the inclusion of compartment models, our method successfully characterizes the WM lesion with much reduced magnitude of the FODs over these voxels. This is further illustrated in Fig. 10(c) where we plotted the fraction of the intra-axonal compartment computed by our method. These results suggest that there is an increase of extra-axonal water content in the WM lesion regions. Using FOD-based tractography, we can also perform connectivity analysis to investigate possible disruption of

brain functions due to the WM lesion. In summary, this experiment demonstrates the potential of our method for clinically feasible connectivity research based on multi-shell diffusion imaging.

V. Discussions and Conclusions

In this paper, we developed a novel approach for the analysis of multi-shell diffusion imaging data. The main novelty of our method is the incorporation of compartment models into FOD reconstruction to fully utilize the rich information in the multi-shell data. The numerical optimization in our method is easy to implement that consists of the iterative application of a quadratic programming step and a gradient descent step. In our experiments, we compared with DSI-Studio and BEDPOSTX of FSL on simulated and HCP data and demonstrated that our method achieved better performance in FOD reconstruction. Using both HCP and clinical data, we also demonstrated in our experiments that our method not only produces sharp FODs but also generates compartment parameters that have great potentials in the clinical study of WM lesions.

With multi-shell HARDI data, we demonstrated in this work the incorporation of parametric compartment models into the FOD reconstruction process. This allows the *whole brain* analysis of fiber crossings and compartment parameters. Our work is closely related to the ball-stick model that was widely used as part of the FSL software. The main limitation of the ball-stick model, however, is the assumption that the intra-and extra-axonal compartments have the same diffusivity. Our model estimates the FOD and allows the diffusivity of the extra-axonal compartment to be calculated adaptively independent of the diffusivity of the intra-axonal model. We also include a third compartment that takes into account trapped water with no diffusion. Overall our method demonstrated better performance than the ball-stick model in reconstructing fiber direction distributions in the presence of crossing fibers.

There is also much room for further improving our method by incorporating more sophisticated compartment models, especially for the extra-axonal compartment. In a recent study by Ferizi et al. [49], various combinations of compartment models were evaluated at the corpus callosum. Because the fiber directions were assumed known *a priori* and used to select the voxels of interest, the focus of this study was on ranking the models in terms of how well they fit the diffusion signals from 32 shells. While our goal is to resolve fiber crossings in whole brain study, the conclusion of this study are very informative. The reassuring thing is that the top ranked model has three compartments including the stick and dot compartment that are also part of our model. On the other hand, the tensor model performed best for the extra-axonal compartment. Recent work by Xu et al. [63] on postmortem rat spinal cord also suggested the need of anisotropic models for the extra-axonal compartment. There are, however, computational challenges to disentangle the contributions from the intra-axonal compartment and the anisotropic, extra-axonal compartment. This is exemplified by the much lower than expected volume fractions of the intra-axonal compartment for top-ranked models in [49]. It will be even more challenging for voxels with complicated fiber configurations. In our current method, we use the stick kernel and FOD to absorb contributions to the signal from anisotropic diffusion and let the other two compartments represent the rest of the signal. We showed that our model can

provide high quality fitting to the diffusional imaging signals in the presence of fiber crossings and applied it to whole brain study for the reconstruction of fiber bundles. To incorporate the full tensor model into the extra-axonal compartment, it is important to carefully consider its interference with FOD estimation because both models with try to explain the anisotropy in water diffusion. One critical direction is thus to investigate the optimal image acquisition protocols that can resolve this ambiguity. For the study of Ferizi et al. [49], 250 runs of a numerical algorithm were used to obtain the best fit. There is thus clearly also a need of more tractable computational algorithms for the reliable estimation of FODs and parameters from more sophisticated compartment models.

For future work, we will also perform more extensive validations on both the HCP data and multi-shell imaging data of brain diseases. We will perform more comprehensive fiber bundle extractions with the FODs computed from HCP data and construct high quality atlases for the analysis of clinical imaging data. We will also investigate the application of the compartment parameters in the early detection of WM changes before they appear in conventional T2-FLAIR images.

Acknowledgments

This work was in part supported by the National Institute of Health (NIH) under Grant K01EB013633, P41EB015922, P50AG005142. Also Giang Tran would acknowledge the support of the W. M. Keck Foundation.

Data used in this paper were provided in part by the Human Connectome Project, WU-Minn Consortium (Principal Investigators: David Van Essen and Kamil Ugurbil; 1U54MH091657) funded by the 16 NIH Institutes and Centers that support the NIH Blueprint for Neuroscience Research; and by the McDonnell Center for Systems Neuroscience at Washington University.

References

1. Basser J, Mattiello PJ, LeBihan D. MR diffusion tensor spectroscopy and imaging. Biophys J. 1994; 66(1):259–267. [PubMed: 8130344]
2. Mori S, Crain BJ, Chacko V, Van Zijl P. Three-dimensional tracking of axonal projections in the brain by magnetic resonance imaging. Annals of neurology. 1999; 45(2):265–269. [PubMed: 9989633]
3. Basser PJ, Pajevic S, Pierpaoli C, Duda J, Aldroubi A. In vivo fiber tractography using dt-mri data. Magnetic Resonance in Medicine. 2000; 44(4):625–632. [PubMed: 11025519]
4. Parker GJ, Alexander DC. Probabilistic Monte Carlo based mapping of cerebral connections utilising whole-brain crossing fibre information. Proc IPMI. 2003:684–695.
5. Jbabdi S, Woolrich M, Andersson J, Behrens T. A Bayesian framework for global tractography. NeuroImage. 2007; 37(1):116–129. [PubMed: 17543543]
6. Zhang F, Hancock ER, Goodlett C, Gerig G. Probabilistic white matter fiber tracking using particle filtering and von mises-fisher sampling. Medical Image Analysis. 2009; 13(1):5–18. [PubMed: 18602332]
7. Tournier JD, Calamante F, Connelly A. Mrtrix: Diffusion tractography in crossing fiber regions. International Journal of Imaging Systems and Technology. 2012; 22(1):53–66.
8. Wedeen VJ, Rosene DL, Wang R, Dai G, Mortazavi F, Hagmann P, Kaas JH, Tseng WYI. The geometric structure of the brain fiber pathways. Science. 2012; 335(6076):1628–1634. [PubMed: 22461612]
9. Catani M, Bodi I, DellAcqua F. Comment on the geometric structure of the brain fiber pathways. Science. 2012; 337(6102):1605. [PubMed: 23019632]
10. Jansons KM, Alexander DC. Persistent angular structure: new insights from diffusion magnetic resonance imaging data. Inverse problems. 2003; 19(5):1031.

11. Tuch DS, Reese TG, Wiegell MR, Makris N, Belliveau JW, Wedeen VJ. High angular resolution diffusion imaging reveals intravoxel white matter fiber heterogeneity. Magnetic Resonance in Medicine. 2002; 48(4):577–582. [PubMed: 12353272]
12. Tuch DS. Q-ball imaging. Magnetic Resonance in Medicine. 2004; 52(6):1358–1372. [PubMed: 15562495]
13. Liu C, Bammer R, Acar B, Moseley ME. Characterizing non-gaussian diffusion by using generalized diffusion tensors. Magnetic Resonance in Medicine. 2004; 51(5):924–937. [PubMed: 15122674]
14. Özarslan E, Shepherd TM, Vemuri BC, Blackband SJ, Mareci TH. Resolution of complex tissue microarchitecture using the diffusion orientation transform (dot). NeuroImage. 2006; 31(3):1086–1103. [PubMed: 16546404]
15. Anderson AW. Measurement of fiber orientation distributions using high angular resolution diffusion imaging. Magnetic Resonance in Medicine. 2005; 54(5):1194–1206. [PubMed: 16161109]
16. Tournier J, Calamante F, Connelly A. Robust determination of the fibre orientation distribution in diffusion MRI: non-negativity constrained super-resolved spherical deconvolution. NeuroImage. 2007; 35(4):1459–1472. [PubMed: 17379540]
17. Jian B, Vemuri BC. A unified computational framework for deconvolution to reconstruct multiple fibers from diffusion weighted MRI. IEEE Trans Med Imag. 2007; 26(11):1464–1471.
18. Tournier J, Yeh C-H, Calamante F, Cho K-H, Connelly A, Lin C-P, et al. Resolving crossing fibres using constrained spherical deconvolution: validation using diffusion-weighted imaging phantom data. Neuroimage. 2008; 42(2):617–625. [PubMed: 18583153]
19. Descoteaux M, Deriche R, Knosche T, Anwander A. Deterministic and probabilistic tractography based on complex fibre orientation distributions. IEEE Trans Med Imag. 2009; 28(2):269–286.
20. Dell'Acqua F, Scifo P, Rizzo G, Catani M, Simmons A, Scotti G, Fazio F. A modified damped Richardson Lucy algorithm to reduce isotropic background effects in spherical deconvolution. NeuroImage. 2010; 49(2):1446–1458. [PubMed: 19781650]
21. Patel V, Shi Y, Thompson PM, Toga AW. Mesh-based spherical deconvolution: A flexible approach to reconstruction of nonnegative fiber orientation distributions. NeuroImage. 2010; 51(3):1071–1081. [PubMed: 20206705]
22. Ugurbil K, Xu J, Auerbach EJ, Moeller S, Vu AT, Duarte-Carvajalino JM, Lenglet C, Wu X, Schmitter S, de Moortele PFV, Strupp J, Sapiro G, Martino FD, Wang D, Harel N, Garwood M, Chen L, Feinberg DA, Smith SM, Miller KL, Sotiropoulos SN, Jbabdi S, Andersson JL, Behrens TE, Glasser MF, Essen DCV, Yacoub E. Pushing spatial and temporal resolution for functional and diffusion MRI in the Human Connectome Project. NeuroImage. 2013; 80:80–104. [PubMed: 23702417]
23. Sotiropoulos SN, Jbabdi S, Xu J, Andersson JL, Moeller S, Auerbach EJ, Glasser MF, Hernandez M, Sapiro G, Jenkinson M, Feinberg DA, Yacoub E, Lenglet C, Essen DCV, Ugurbil K, Behrens TE. Advances in diffusion MRI acquisition and processing in the Human Connectome Project. NeuroImage. 2013; 80(0):125–143. [PubMed: 23702418]
24. Feinberg DA, Moeller S, Smith SM, Auerbach E, Ramanna S, Glasser MF, Miller KL, Ugurbil K, Yacoub E. Multiplexed echo planar imaging for sub-second whole brain fmri and fast diffusion imaging. PLoS ONE. 2010; 5(12):e15710. [PubMed: 21187930]
25. Moeller S, Yacoub E, Olman CA, Auerbach E, Strupp J, Harel N, Uurbil K. Multiband multislice ge-epi at 7 tesla, with 16-fold acceleration using partial parallel imaging with application to high spatial and temporal whole-brain fmri. Magnetic Resonance in Medicine. 2010; 63(5):1144–1153. [PubMed: 20432285]
26. Setsompop K, Gagoski BA, Polimeni JR, Witzel T, Wedeen VJ, Wald LL. Blipped-controlled aliasing in parallel imaging for simultaneous multislice echo planar imaging with reduced g-factor penalty. Magnetic Resonance in Medicine. 2012; 67(5):1210–1224. [PubMed: 21858868]
27. Essen DV, Ugurbil K, et al. The human connectome project: A data acquisition perspective. NeuroImage. 2012; 62(4):2222–2231. [PubMed: 22366334]
28. Toga A, Clark K, Thompson P, Shattuck D, Van Horn J. Mapping the human connectome. Neurosurgery. 2012; 71(1):1–5. [PubMed: 22705717]

29. Wedeen VJ, Hagmann P, Tseng WYI, Reese TG, Weisskoff RM. Mapping complex tissue architecture with diffusion spectrum magnetic resonance imaging. Magnetic Resonance in Medicine. 2005; 54(6):1377–1386. [PubMed: 16247738]
30. Wu YC, Alexander AL. Hybrid diffusion imaging. NeuroImage. 2007; 36(3):617–629. [PubMed: 17481920]
31. Descoteaux M, Deriche R, Le Bihan D, Mangin JF, Poupon C. Multiple q-shell diffusion propagator imaging. Medical image analysis. 2011; 15(4):603–621. [PubMed: 20685153]
32. Scherrer B, Warfield SK. Parametric representation of multiple white matter fascicles from cube and sphere diffusion mri. PLoS ONE. 2012; 7(11)
33. Rathi Y, Michailovich O, Laun F, Setsompop K, Grant P, Westin C-F. Multi-shell diffusion signal recovery from sparse measurements. Medical Image Analysis. 2014; 18(7):1143–1156. [PubMed: 25047866]
34. Aganj I, Lenglet C, Sapiro G, Yacoub E, Ugurbil K, Harel N. Reconstruction of the orientation distribution function in single- and multiple-shell q-ball imaging within constant solid angle. Magnetic Resonance in Medicine. 2010; 64(2):554–566. [PubMed: 20535807]
35. Assaf Y, Freidlin RZ, Rohde GK, Basser PJ. New modeling and experimental framework to characterize hindered and restricted water diffusion in brain white matter. Magnetic Resonance in Medicine. 2004; 52(5):965–978. [PubMed: 15508168]
36. Assaf Y, Basser PJ. Composite hindered and restricted model of diffusion (CHARMED) MR imaging of the human brain. Neuroimage. 2005; 27(1):48–58. [PubMed: 15979342]
37. Stanisz GJ, Wright GA, Henkelman RM, Szafer A. An analytical model of restricted diffusion in bovine optic nerve. Magnetic Resonance in Medicine. 1997; 37(1):103–111. [PubMed: 8978638]
38. Jespersen SN, Kroenke CD, Østergaard L, Ackerman JJ, Yablonskiy DA. Modeling dendrite density from magnetic resonance diffusion measurements. Neuroimage. 2007; 34(4):1473–1486. [PubMed: 17188901]
39. Assaf Y, Blumenfeld-Katzir T, Yovel Y, Basser PJ. Axcaliber: A method for measuring axon diameter distribution from diffusion MRI. Magnetic Resonance in Medicine. 2008; 59(6):1347–1354. [PubMed: 18506799]
40. Barazany D, Basser PJ, Assaf Y. In vivo measurement of axon diameter distribution in the corpus callosum of rat brain. Brain. 2009; 132(5):1210–1220. [PubMed: 19403788]
41. Alexander DC, Hubbard PL, Hall MG, Moore EA, Ptito M, Parker GJ, Dyrby TB. Orientationally invariant indices of axon diameter and density from diffusion MRI. NeuroImage. 2010; 52(4):1374–1389. [PubMed: 20580932]
42. Zhang H, Hubbard PL, Parker GJ, Alexander DC. Axon diameter mapping in the presence of orientation dispersion with diffusion MRI. NeuroImage. 2011; 56(3):1301–1315. [PubMed: 21316474]
43. Zhang H, Schneider T, Wheeler-Kingshott CA, Alexander DC. NODDI: Practical in vivo neurite orientation dispersion and density imaging of the human brain. NeuroImage. 2012; 61(4):1000–1016. [PubMed: 22484410]
44. Assaf Y, Alexander DC, Jones DK, Bizzi A, Behrens TE, Clark CA, Cohen Y, Dyrby TB, Huppi PS, Knoesche TR, LeBihan D, GJM, Poupon C. The CONNECT project: Combining macroand micro-structure. NeuroImage. 2013; 80:273–282. [PubMed: 23727318]
45. Behrens T, Woolrich M, Jenkinson M, Johansen-Berg H, Nunes R, Clare S, Matthews P, Brady J, Smith S. Characterization and propagation of uncertainty in diffusion-weighted mr imaging. Magnetic resonance in medicine. 2003; 50(5):1077–1088. [PubMed: 14587019]
46. Behrens T, Berg HJ, Jbabdi S, Rushworth M, Woolrich M. Probabilistic diffusion tractography with multiple fibre orientations: What can we gain? NeuroImage. 2007; 34(1):144–155. [PubMed: 17070705]
47. Jbabdi S, Sotiropoulos SN, Savio AM, Graa M, Behrens TEJ. Model-based analysis of multishell diffusion mr data for tractography: How to get over fitting problems. Magnetic Resonance in Medicine. 2012; 68(6):1846–1855. [PubMed: 22334356]
48. Panagiotaki E, Schneider T, Siow B, Hall MG, Lythgoe MF, Alexander DC. Compartment models of the diffusion MR signal in brain white matter: a taxonomy and comparison. Neuroimage. 2012; 59(3):2241–2254. [PubMed: 22001791]

49. Ferizi U, Schneider T, Panagiotaki E, Nedjati-Gilani G, Zhang H, Wheeler-Kingshott CAM, Alexander DC. A ranking of diffusion mri compartment models with in vivo human brain data. Magnetic Resonance in Medicine. 2014; 72(6):1785–1792. [PubMed: 24347370]
50. Yeh FC, Wedeen VJ, Tseng WYI. Estimation of fiber orientation and spin density distribution by diffusion deconvolution. NeuroImage. 2011; 55(3):1054–1062. [PubMed: 21232611]
51. Yeh FC, Wedeen VJ, Tseng WY. Generalized-sampling imaging. IEEE Trans Med Imag. 2010; 29(9):1626–1635.
52. Tran G, Shi Y. Adaptively constrained convex optimization for accurate fiber orientation estimation with high order spherical harmonics. Proc MICCAI. 2013:485–492.
53. Cheng J, Deriche R, Jiang T, Shen D, Yap P-T. Non-negative spherical deconvolution (NNSD) for estimation of fiber orientation distribution function in single-/multi-shell diffusion MRI. NeuroImage. 2014; 101:750–764. [PubMed: 25108182]
54. Jeurissen B, Tournier JD, Dhollander T, Connelly A, Sijbers J. Multi-tissue constrained spherical deconvolution for improved analysis of multi-shell diffusion MRI data. NeuroImage. 2014; 103(0):411–426. [PubMed: 25109526]
55. Peyré G, Cohen L. Geodesic remeshing using front propagation. International Journal of Computer Vision. 2006; 69(1):145–156.
56. Wills, A. QPC-Quadratic programming in C. [Online]. Available: http://sigpromu.org/quadprog/index.html
57. Shi Y, Lai R, Toga A. Cortical surface reconstruction via unified Reeb analysis of geometric and topological outliers in magnetic resonance images. IEEE Trans Med Imag. 2013; (3):511–530.
58. Shi Y, Lai R, Wang D, Pelletier D, Mohr D, Sicotte N, Toga A. Metric optimization for surface analysis in the laplace-beltrami embedding space. IEEE Trans Med Imag. 2014; 33(7):1447–1463.
59. Shattuck D, Mirza M, Adisetiyo V, Hojatkashani C, Salamon G, Narr K, Poldrack R, Bilder R, Toga A. Construction of a 3D probabilistic atlas of human brain structures. NeuroImage. 2008; 39(3):1064–1080. [PubMed: 18037310]
60. Sethian J. A fast marching level set method for monotonically advancing fronts. Proc Nat Acad Sci. 1996; 93(4):1591–1595. [PubMed: 11607632]
61. Zhang Y, Zhang J, Oishi K, Faria AV, Jiang H, Li X, Akhter K, Rosa-Neto P, Pike GB, Evans A, Toga AW, Woods R, Mazziotta JC, Miller MI, van Zijl PC, Mori S. Atlas-guided tract reconstruction for automated and comprehensive examination of the white matter anatomy. NeuroImage. 2010; 52(4):1289–1301. [PubMed: 20570617]
62. Catani, M.; de Schotten, MT. Atlas of Human Brain Connections. Oxford University Press; 2012.
63. Xu J, Li H, Harkins KD, Jiang X, Xie J, Kang H, Does MD, Gore JC. Mapping mean axon diameter and axonal volume fraction by MRI using temporal diffusion spectroscopy. NeuroImage. 2014; 103(0):10–19. [PubMed: 25225002]

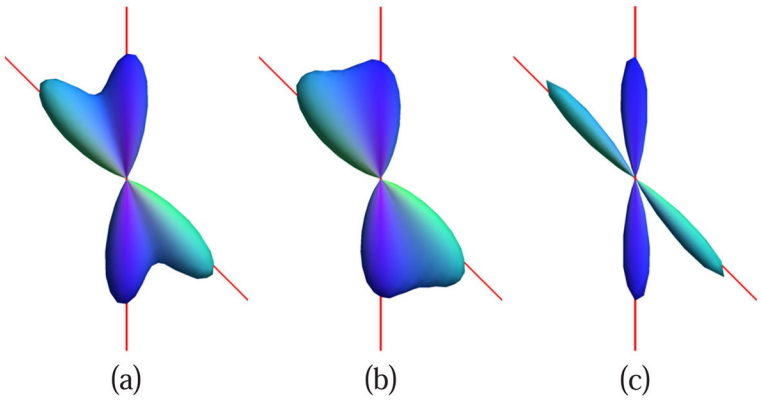

Fig. 1.

Impact of non-negative constraints on FOD reconstruction. True fiber directions are plotted as red lines. (a) SPHARM order $L = 8$; num of constraints $M = 69$. (b) SPHARM order $L = 8$; num of constraints $M = 100$. (c) SPHARM order $L = 16$; num of constraints $M = 216$.

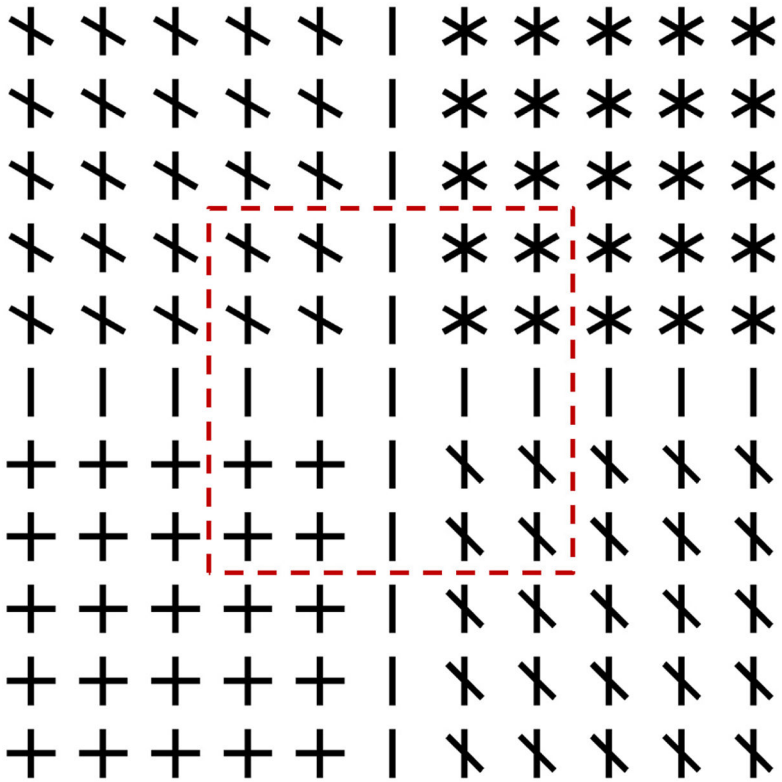

Fig. 2.
Simulated fiber directions.

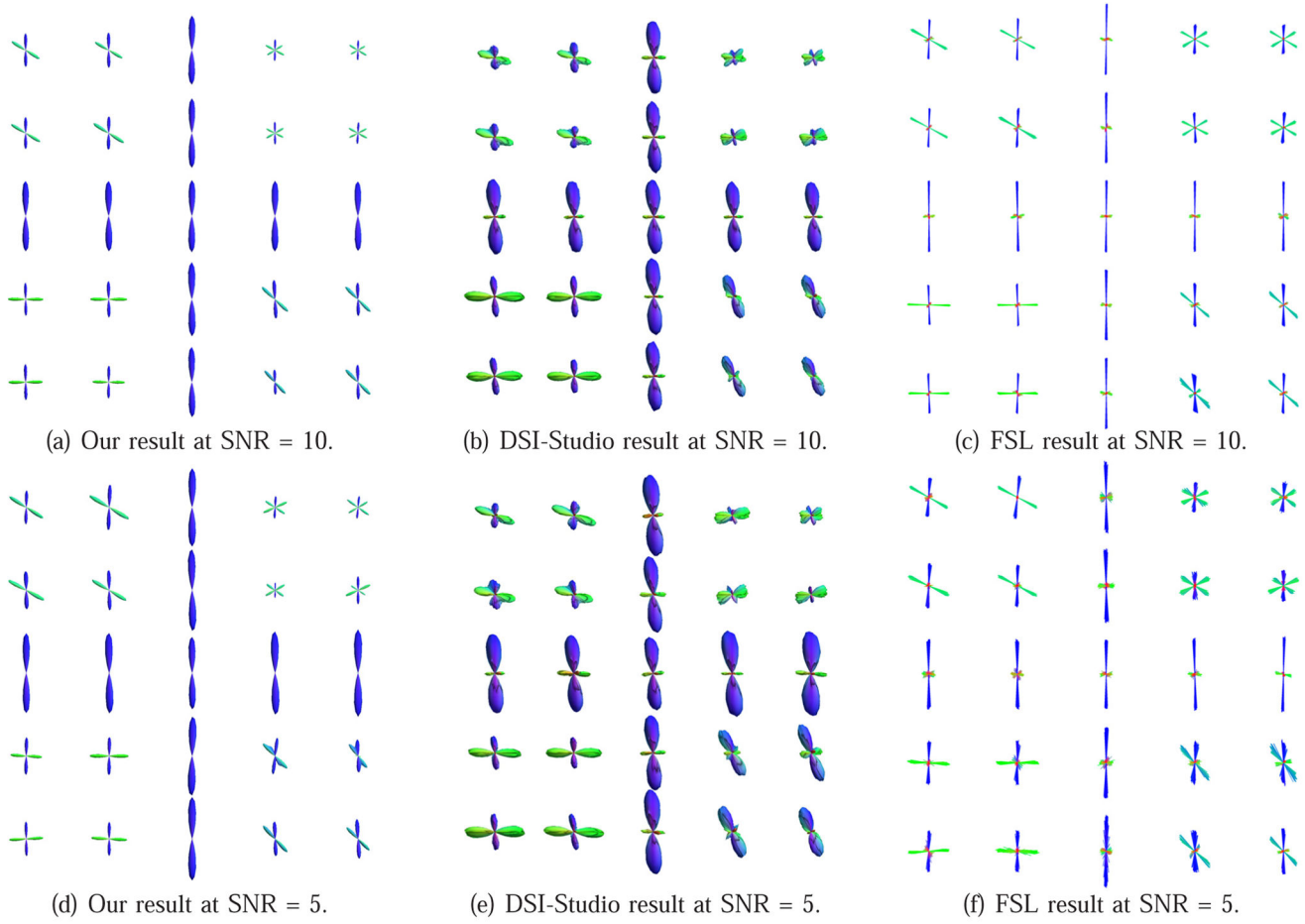

Fig. 3.

A comparison of our method with DSI-Studio and BEDPOSTX of FSL using simulated diffusion imaging signal.

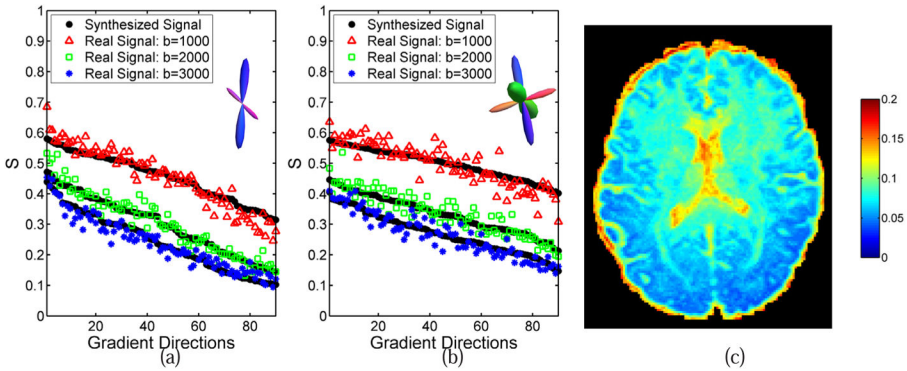

Fig. 4.

A comparison of the real signal and the synthesized signal with our three-compartment model using the reconstructed FOD and compartment parameters. The excellent match demonstrates the validity of our model. (a)(b) Synthesized vs real signal at two voxels. (c) Ratio between the norm of the residue and signal on an axial slice.

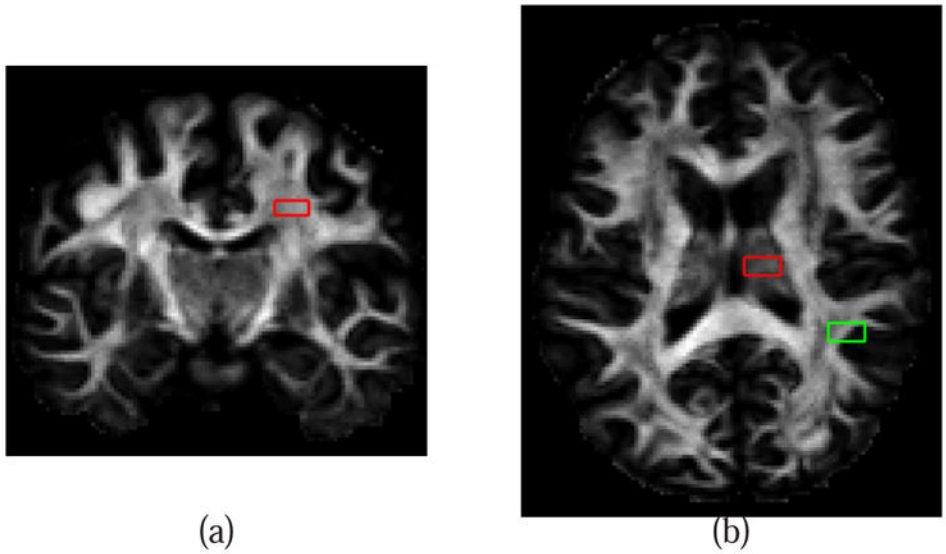

Fig. 5.

Representative ROIs used for comparisons of FOD reconstruction. (a) ROI I (red) on the coronal slice is in the WM region. (b) ROI II and III are on the axial slice with ROI II (red) in the thalamus and ROI III (green) on the GM and WM boundary.

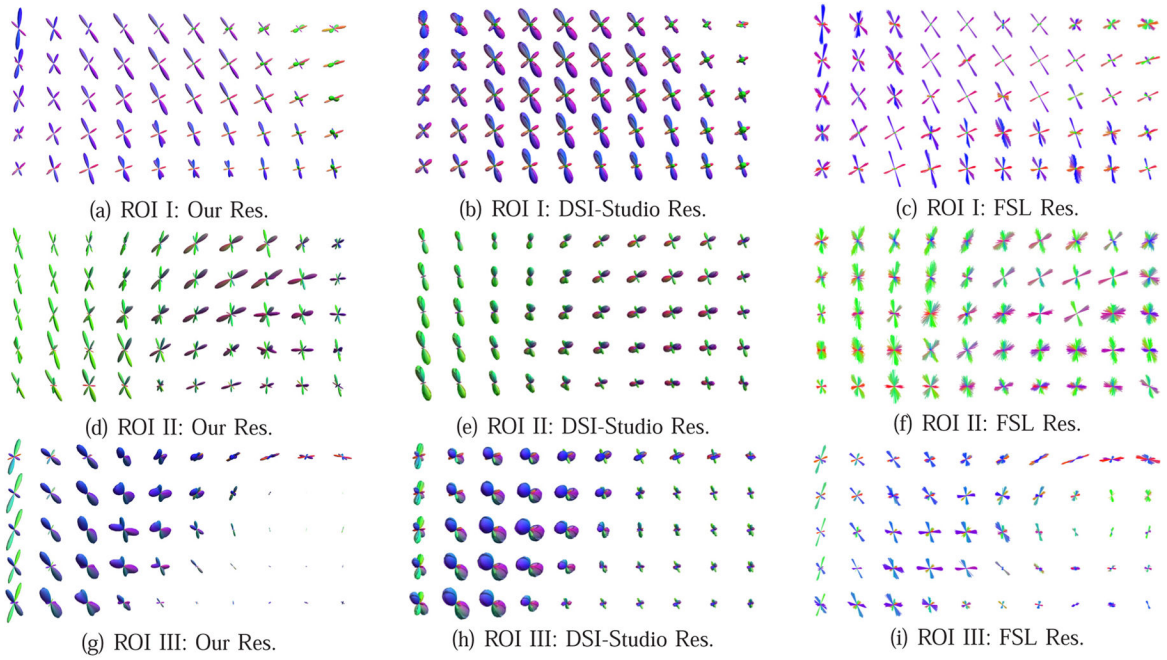

Fig. 6.

A comparison of the FODs reconstructed by our method and DSI-Studio, and the fiber directions by BEDPOSTX of FSL in the three ROIs shown in Fig. 5.

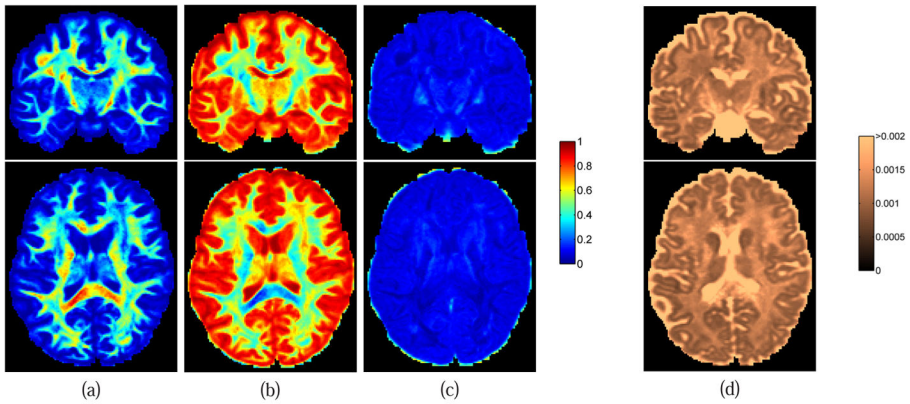

Fig. 7.

The compartment models estimated by our new method are plotted on an axial and coronal slice. (a) Intra-axonal fraction: integral of the FOD. (b) Extra-axonal fraction: α. (c) Trapped water fraction: γ. (d) Diffusivity of the extra-axonal compartment: λ_{iso}. Note the separation of white and gray matter by the diffusivity of the extra-axonal compartment in (d).

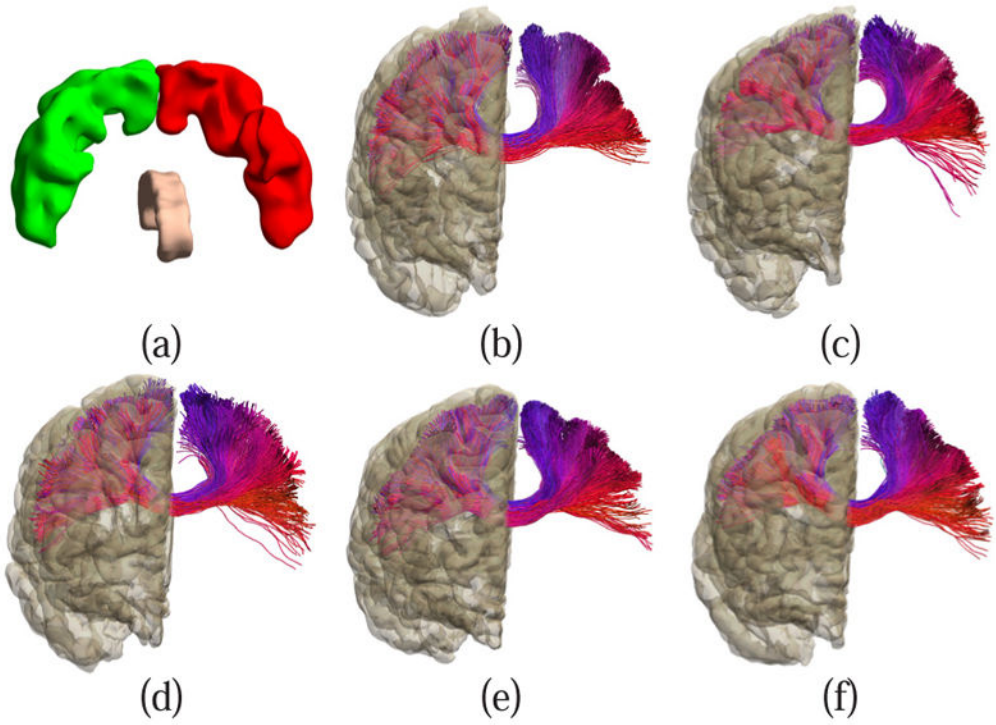

Fig. 8.

Corpus callosum bundle that connects the precentral gyrus of left and right hemispheres. (a) Seed regions for corpus callosum bundle reconstruction: left precentral gyrus (red); right precentral gyrus (green); middle sagittal slices of CC (brown). (b)-(f) Examples of corpus callosum bundle overlaid with the right hemispherical cortical surface from five subjects.

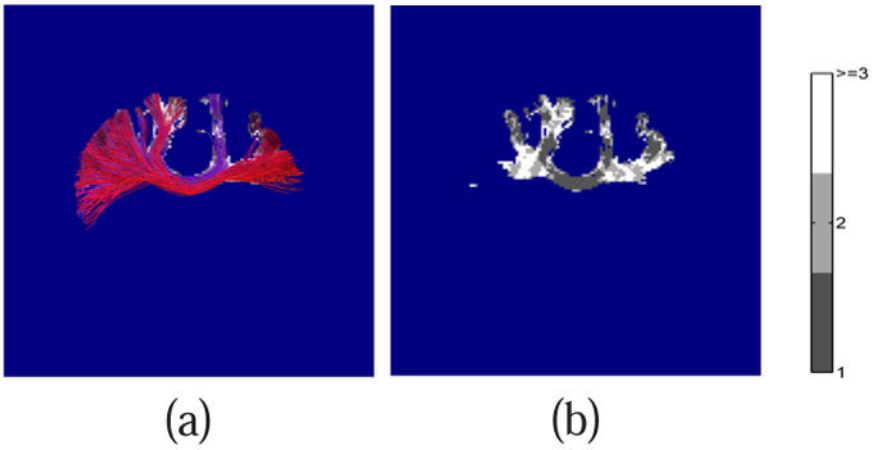

Fig. 9.

An illustration of the regions with crossing fibers that the CC bundle passes through. The background is plotted in blue. (a) Overlay of the CC bundle and one coronal slice of the peak image. (b) The corresponding coronal slice of the peak image.

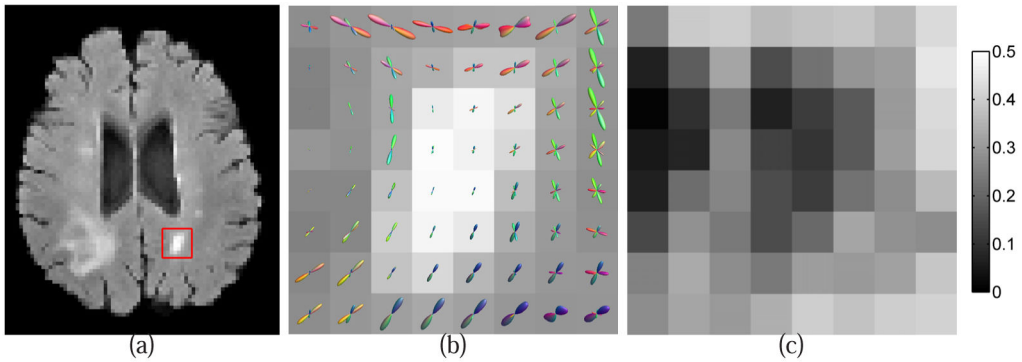

Fig. 10.

An illustration of FOD-based analysis of WM lesions. (a) WM lesions on an axial slice of a T2-FLAIR image. The ROI is highlighted with the red box. (b) FODs are overlaid on top of the T2-FLAIR image in the ROI. (c) Intra-axonal fraction of the ROI computed by our method.

TABLE I

Reconstruction Algorithm

Set $\xi = \xi_{init}$, and $M = M_{init}$.

1 Iteratively increase M and solve (15) until (18) is satisfied.

2 Repeat the following steps until convergence.

2.1 Update λ_{iso} in the gradient descent direction according to (16).

2.2 Iteratively increase M and solve (15) until (18) is satisfied.

3 If FOD sparsity is satisfied, stop the iteration. Otherwise, set $\xi = \xi + \delta_{\xi}$ and go back to Step 1.

TABLE II

Average angular errors (mean±std).

	Our Method	DSI-Studio	FSL
SNR=10	9.3º ± 0.40º	25.01º ± 3.78º	16.89º ± 4.05º
SNR=5	9.8º ± 0.76º	26.32º ± 4.02º	17.08º ± 4.17º

TABLE III

Compartment parameter estimation errors. (mean±std).

	$\int f$	a	γ	λ_{iso}
SNR=10	0.0053 ± 0.02	0.0036 ± 0.012	0.0031 ± 0.0095	$-0.072 \times 10^{-4} \pm 0.39 \times 10^{-4}$
SNR=5	0.015 ± 0.028	−0.003 ± 0.0175	−0.0002 ± 0.0175	$-0.042 \times 10^{-4} \pm 0.65 \times 10^{-4}$

TABLE IV

Statistics about the peak image of CC bundles: percentile of voxels containing different numbers of fiber directions ($K = 1, 2, \geq 3$). Only voxels that CC bundles passing through are considered.

	$K = 1$	$K = 2$	$K \geq 3$
Subject 1	38.1%	33.4%	28.5%
Subject 2	33.6%	32.5%	33.9%
Subject 3	37.2%	32.9%	29.9%
Subject 4	40.2%	29.2%	30.6%
Subject 5	40.0%	31.5%	28.5%